

Sea Ice Transition Detection Using Incoherent Integration and Deconvolution

Benjamin J. Southwell , *Student Member, IEEE*, and Andrew G. Dempster , *Senior Member, IEEE*

Abstract—Currently, reflectometry-based sea ice detection methods rely on observables extracted from delay-Doppler maps (DDM)s, which are sensitive to ice in the specular zone. Due to the size of the glistening zone, the transition from open seas to sea ice in the specular zone can take up to 10 s for satellite platforms and no methods exist that can process this. In this article, using DDMs collected by TechDemoSat-1, we demonstrate that this transition is comprised of a response that is fixed in the spatial domain, at the ice edge, and moving in the delay-Doppler domain. This is the first observation of persistent nonspecular coherent reflections from sea ice. The delay-Doppler trajectory of the ice response is shown to correspond with a point that is located on the ambiguity free line. Furthermore, the response is point-like as it suffers from delay and Doppler walk suggesting that it originates from a small spatial footprint, i.e., the first (few) Fresnel zone(s). Exploiting these facts, we then propose a technique that integrates the ice response in the spatial domain after preprocessing. This results in the edges of the ice sheet being emphasized as all of the power received during the transition phase maps to the edge of the sheet. We also propose to compensate for the delay-Doppler walk during preprocessing by modifying Woodward’s ambiguity function when deconvolution is performed.

Index Terms—GNSS-R, reflectometry, sea ice, transition, ice detection.

I. INTRODUCTION

EARLY work demonstrated that detecting sea ice using airborne [1], [2] and spaceborne (UK-DMC) [3] GNSS-R receivers was possible. During this work, it was found that the response of ice in the delay-Doppler map (DDM) has a high signal-to-noise ratio (SNR) and little to no spreading due to the coherent nature of ice reflections. Coherent reflections are thought to originate from the first Fresnel zone [4], which for the spaceborne receiver, is on the order of ≈ 500 – 1000 m [5] compared to the typical size of $t \approx 20$ km depending on geometry.

Using multiple observables extracted from the specular zone, Yan and Huang [6] presented a method for sea ice detection in DDMs collected by TechDemoSat-1 (TDS-1). These observables describe the spread of the signal, and, if the DDM does not present a significant spread, it is classified as an ice

reflection. Additionally, they incoherently average DDMs in order to improve the SNR. The number of DDMs averaged, $M \in [1, \dots, 20]$, is adaptively chosen, resulting in poor spatial resolution due to the $\approx M \times 6$ km of along-track blurring caused by the motion of the receiver and specular point. Other than the adaptive incoherent averaging, in a similar fashion [7] extracts multiple observables from DDMs collected by TDS-1. These include a matched filter output wherein the DDM is correlated with a replica specular impulse response. For GNSS-R receivers, this impulse response is Woodward’s ambiguity function [8], χ^2 , which for DDMs collected by TDS-1 can be approximated as [9]:

$$\chi^2(\Delta\tau, \Delta f_D) \simeq \Lambda^2(\Delta\tau) \text{Sinc}^2(\Delta f_D) \quad (1)$$

where $\Delta\tau = \bar{\tau} - \tau$; $\Delta f_D = \bar{f}_D - f_D$; $(\bar{\tau}, \bar{f}_D)$ are the delay Doppler (DD) coordinates of the DDM; and (τ, f_D) is the actual DD coordinates of some response. DDMs that correlate highly with the specular χ^2 response are termed “K” DDMs by [7] due to the shape of the power envelope surface and are classified as ice reflections. Again, this method is only sensitive to ice in the specular zone and does not handle the transition from open seas to specular ice reflections.

The transition phase is significant as the time it takes a point fixed on the ground (e.g., the ice edge) to traverse from the outskirts of the glistening zone (GZ) to the specular point can be up to ≈ 10 s [10]. Therefore, methods that do not handle the transition phase cannot process the sea ice response for $\approx 10 \times 6$ km = 60 km along the surface.

The detection of the transition from open waters to ice has been demonstrated recently [11], [12]. In [11], a transition is detected by extracting observables from a first difference of contiguous DDMs. They also employ the adaptive incoherent integration method from [6] and as a result, also suffer from poor spatial resolution. Conversely, Schiavulli *et al.* [12] detect transitions in the spatial domain. This is done by deconvolving the DDM before transforming it back to the spatial domain where the transition is detected by a peak response away from the specular zone in the radar image corresponding to the entry of the ice sheet’s edge into the GZ. However, this article only processes a single epoch and does not exploit the nature of the transitioning response.

In this article, we present a method that supports detection of sea ice including the transition, i.e., the ice edge. We do so by incoherently integrating an arbitrary number of DDMs without inducing any blurring. This is achieved by performing the integration in the spatial domain after the sea clutter has been

Manuscript received June 11, 2019; revised August 20, 2019; accepted September 20, 2019. Date of publication October 10, 2019; date of current version February 12, 2020. This work was supported by the Australian Government through the Research Training Program. (*Corresponding author: Benjamin Southwell.*)

The authors are with the Australian Centre for Space Engineering Research, University of New South Wales, Sydney NSW 2052, Australia (e-mail: b.southwell@unsw.edu.au; a.dempster@unsw.edu.au).

Digital Object Identifier 10.1109/JSTARS.2019.2943510

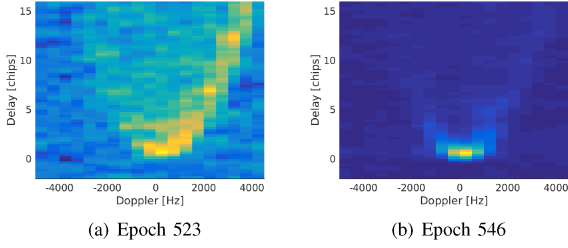


Fig. 1. (a) DDM that was collected immediately before the ice enters the GZ. This contains only a sea clutter response and is representative of DDMs collected at epochs 522 to 529. (b) DDM from the sequence containing a specular ice-only response. This is representative of DDMs collected at epochs 539 through 564. During the specular ice-only phase, the ice response comes from the specular point, which is moving in the spatial domain and stationary in the DD domain.

suppressed and the DDM deconvolved to remove the effect of χ^2 . Furthermore, we compensate for the spatially variant blurring of χ^2 [13] in the DD domain during the deconvolution process. Using this method, it is possible to construct ice sheet maps using different receivers, specular point tracks and temporally separate (within reason) DDMs as the integration is performed in the spatial domain. Furthermore, we will show that an extended ice sheet has an unambiguous response allowing us to map power to the spatial domain in a straight-forward manner. Moreover, during the transition from open seas to ice, we find that the response of the ice sheet comes from a point fixed on the ambiguity free line (AFL) with a small spatial footprint. This is the first observation of persistent nonspecular scattering off sea ice in GNSS-R observables.

II. SEA ICE IN DDM SEQUENCES

In this article, we analyze and process DDMs collected by TDS-1 on April 01, 2015, specifically those in H00 group 95. Epochs are equivalent to the netCDF file group indexes. The DDMs in this sequence can be classified as either only sea clutter, mixed DDMs containing sea clutter and a transitioning ice response or specular ice-only DDMs.

Fig. 1(a) depicts the DDM collected at epoch 523. This DDM contains only a diffuse sea clutter response and is typical of DDMs collected over open seas. This DDM is representative of all DDMs collected at epochs 522 to 529 inclusively. Fig. 1(b) shows the DDM collected at epoch 546 where the DDM is comprised of a specular ice-only response. This DDM is representative of all DDMs collected at epochs 539 to 564 inclusively. The transition from open seas to an ice sheet occurs during epochs 530 to 538. Fig. 2 shows DDMs collected during this transition phase. These DDMs contain a strong coherent response that can be seen to traverse along the AFL down to the specular point. After the response moves to the specular zone, there are 25 contiguous DDMs similar to Fig. 1(b). Then, the specular sea ice response gives way as the response moves from the specular zone along the AFL toward negative Dopplers. This is shown in Fig. 3.

A fixed point on the surface that coincides with the specular point moves along the AFL in the DD domain (\approx leading edge of the DDM [14]) from positive to negative Doppler frequencies in a sequence of DDMs. This suggests that the response of the

ice sheet in the mixed DDMs during its transition phase has a DD trajectory that is consistent with a point that is fixed on the surface. Once the ice response is specular, the reflection comes from the moving specular point. During the second mixed phase the response moves along the AFL toward negative Dopplers, again consistent with a fixed point. These observations indicate that the fixed points associated with each of the transition phases are in fact the edges of the ice sheet. This hypothesis requires that persistent nonspecular scattering occurs off sea ice.

Each DDM in the sequence of 47 DDMs analyzed and processed in this article is classified according to Table I.

III. DYNAMICS ANALYSIS

Here, we investigate the hypothesis that the ice response during the transition phase originates from a fixed point on the surface. We do this by finding the center of mass of the ice response during the first transition phase to estimate the DD coordinates. These are shown as color scatter plots in Fig. 4. We use a second-order fit for delay and a linear fit for Doppler to match the spatial gradient fields $\nabla\tau$ and ∇f_D , respectively. Using the metadata (bistatic configuration) computed on-board SGR-ReSI, we also compute the DD trajectory of a point located on the AFL. This is shown with the dashed black line. The AFL DD profile was obtained by evaluating the delay

$$\tau(\mathbf{Q}) = \|\mathbf{T} - \mathbf{Q}\| + \|\mathbf{R} - \mathbf{Q}\| \quad (2)$$

and Doppler

$$f_D(\mathbf{Q}) = \frac{-f_0}{c} \left(\dot{\mathbf{T}}^T \hat{\mathbf{m}}(\mathbf{Q}) + \dot{\mathbf{R}}^T \hat{\mathbf{n}}(\mathbf{Q}) \right) \quad (3)$$

by setting \mathbf{Q} to be equal to the specular point at epoch 539 in the supplied metadata. \mathbf{T} is the transmitter's position; \mathbf{R} is the receiver's position; a dot accent indicates a time derivative; f_0 is the L1 center frequency; c is the speed of light; $\hat{\mathbf{m}}$ and $\hat{\mathbf{n}}$ are the normalized antiincident and scattered vectors, respectively.

By taking the first difference of the estimated DD points, we obtain a coarse estimate of the delay change rate (DCR) and Doppler frequency change rate (DFCR) shown as colored scatter plots in Fig. 5. The fits are shown as solid color lines and the AFL rates predicted from the metadata are shown with dashed black lines. The AFL rate estimates were obtained by evaluating the DCR

$$\left. \frac{d\tau}{dt} \right|_{\mathbf{Q}} = -\nabla\tau^T(\mathbf{Q}) \dot{\mathbf{R}}_{\perp} \quad (4)$$

and DFCR

$$\left. \frac{df_D}{dt} \right|_{\mathbf{Q}} = -\nabla f_D^T(\mathbf{Q}) \dot{\mathbf{R}}_{\perp} \quad (5)$$

which were derived in [13].

Looking at Fig. 5, we can see a bias exists between the DFCR estimate extracted from the DDM sequence and what we obtain by analyzing the AFL.

In general, at the end of the transition phase, the ice response does not exactly coincide with the specular point at the integration period boundary and since the delay rate is time variant, this would introduce some error. However, this does not explain

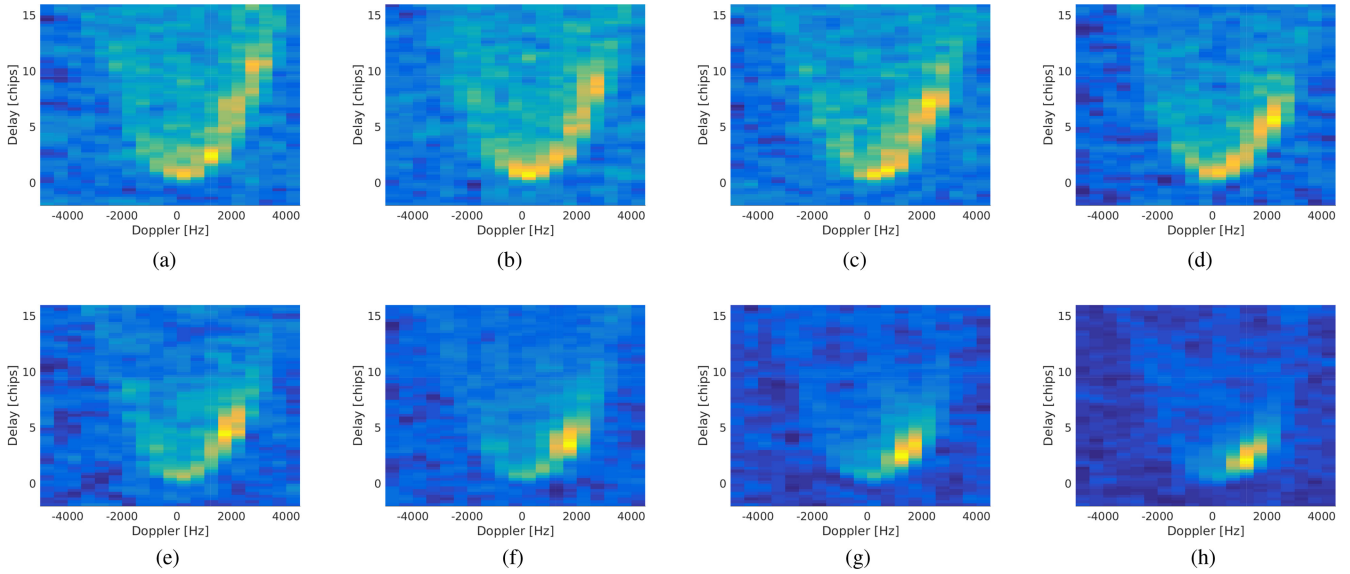


Fig. 2. Mixed DDMs in the first transition phase containing the ice response that originates from a point fixed in the spatial domain and moving in the DD domain. Each DDM is shown on its own color scale as the high dynamic range of the DDMs would result in little contrast within the individual DDMs themselves should they all share the same color scale. This is sufficient as the processing scheme presented in this article normalizes the individual DDMs before combining them. These DDMs were collected when the automatic gain controller was active and are in arbitrary units. (a) Epoch 530. (b) Epoch 531. (c) Epoch 532. (d) Epoch 533. (e) Epoch 534. (f) Epoch 535. (g) Epoch 536. (h) Epoch 537.

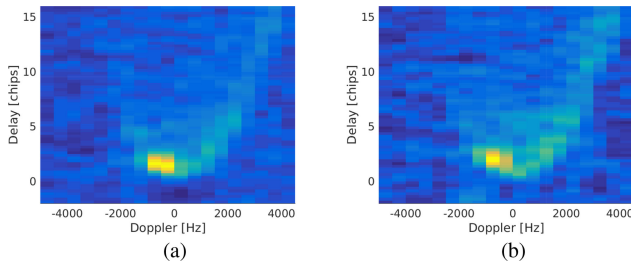


Fig. 3. Mixed DDMs in the second transition phase. In this phase the ice sheet is exiting the GZ and the response comes from a point fixed in the spatial domain but moving in the DD domain. (a) Epoch 566. (b) Epoch 567.

TABLE I
DDM CLASSIFICATION

Epochs	DDM Type	Ice Response
522 - 529	clutter	not present
530 - 538	mixed	moving towards specular DD
539 - 564	ice	located at the specular point
565 - 568	mixed	moving away from specular DD

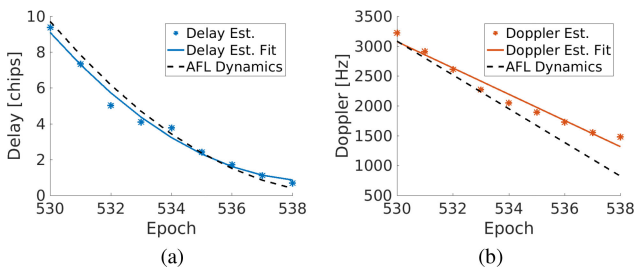


Fig. 4. Estimated DD coordinates of the ice response in the DDM sequence during the transition phase are shown as scatter plots. A fit of each is shown as a solid colored line while the trajectories associated with a fixed point located on the AFL are shown with the dashed black line. (a) Delay. (b) Doppler.

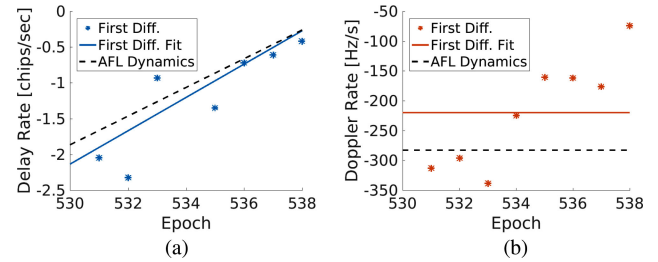


Fig. 5. First difference of the estimate DD coordinates are shown as colored scatter plots. The fits of these, shown with solid colored lines, are used as the estimated DCR and DFCR. The rates associated with a point located on the AFL are shown with the dashed black line. (a) Delay rate. (b) Doppler rate.

the difference in the DFCR. These DDMs were collected at $\approx 47^\circ$ latitude and will suffer from the worst case errors of the quasi-spherical specular point determination method used onboard TDS-1 [15]. Positional errors over 20 km can occur and since the ice is generally not located exactly on the WGS84 ellipsoid these errors may be higher. Large positional offsets introduce both DCR and DFCR errors. Considering that the estimation of the DD coordinate of the ice response is also subject to errors, we can conclude that the ice response observed during the transition period (epochs 530 through 538) originates from a point that is fixed on the Earth's surface. Furthermore, the difference in DCR between the AFL and ice response is proportional to the bias between the DFCRs. This is a property of a fixed point on the surface. Moreover, we can also see that this point is sufficiently close enough to the AFL that the ambiguity problem does not arise.

DDMs produced by SGR-ReSI are formed by tracking the moving specular point, and thus, a point fixed on the surface suffers from significant delay and Doppler walk [13].

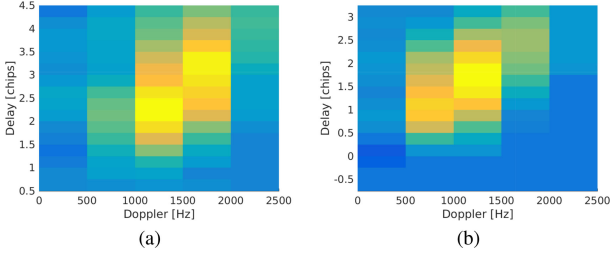


Fig. 6. Zoomed in view of the ice response during the first transition phase. In these DDMs we can clearly see that the response of the ice sheet is suffering from both delay and Doppler walk. This is additional evidence that the scatterer is fixed on the surface. It also suggests the response is coming from a spatial footprint small enough for point-like responses to occur. This is characteristic of a coherent reflection. These DDMs are depicted in arbitrary units on their own colorscales. (a) Epoch 536. (b) Epoch 538.

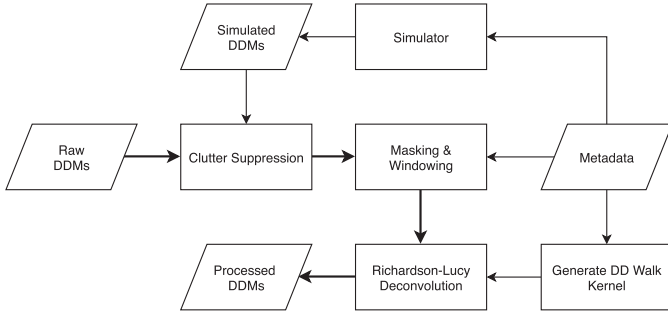


Fig. 7. Flowchart of the DDM processing scheme performed before transformation to the spatial domain.

In Figs. 2 and 3, we can observe this in the response of the transition phase ice response. A zoomed in view of DDMs collected at epochs 536 to 538 inclusively is shown in Fig. 6 where the DD walk can be seen more easily. While being additional evidence that the response comes from a fixed point on the surface, the DD walk is characteristic of a point-liner scatterer where the response originates from the first (few) Fresnel zone(s), i.e., the reflection is coherent.

We can exploit the fact that the ice response maps back to a fixed point during the transition phase by incoherently integrating all of the DDMs in this sequence after transformation back to the spatial domain. This will result in power accumulating at the edge of the ice sheet due to the length of the transition phases. If we continue to integrate power in the spatial domain during the specular ice-only DDMs, we expect the signal power to be blurred along the specular point's track on the surface until the second transition phase occurs at which point the power will then continue to accumulate at the trailing edge of the ice sheet. Furthermore, since the integration is performed in a transmitter and receiver independent frame, DDMs collected by different receivers, PRN tracks and time series can be combined in a manner analogous to collective detection [16] to improve the performance of this technique.

IV. PROCESSING DDMs

Before transformation back to the spatial domain, the DDMs are required to be processed to suppress the clutter and remove any blurring. A flowchart summarizing the DDM processing scheme is shown in Fig. 7. The DDMs are first subjected to

clutter suppression before all of the forbidden cells are masked out and a window is applied to the DDM centered on the ice response. Then, a deconvolution is performed to remove the spreading effect of χ^2 and the relative dynamics of the receiver and ice sheet. After this, the DDM is ready for transformation back to the spatial domain.

Here, we suppress the sea clutter similar to [17]. DDMs are simulated and scaled using the simulator described by [18], [19], before being subtracted from the DDM collected by TDS-1. That is,

$$|Y_{\text{SUP}}(\bar{\tau}, \bar{f}_D, t)|^2 = |\tilde{Y}(\bar{\tau}, \bar{f}_D, t)|^2 - K |Y_{\text{SIM}}(\bar{\tau}, \bar{f}_D, t)|^2 \quad (6)$$

where $|\tilde{Y}|^2$ is the DDM after the noise power has been removed from the received DDM, $|Y|^2$, and

$$|\tilde{Y}(\bar{\tau}, \bar{f}_D, t)|^2 = |Y(\bar{\tau}, \bar{f}_D, t)|^2 - \tilde{P}_N \quad (7)$$

where $|Y_{\text{SIM}}|^2$ is the simulated DDM, K is the scaling factor, $|Y_{\text{SUP}}|^2$ is the DDM with sea clutter suppressed, and \tilde{P}_N is the noise power estimate of $|Y|^2$. Before K can be computed, image registration is performed with a two-dimensional (2-D) correlation of the simulated DDM and the DDM collected by TDS-1. The latter is shifted to align with the peak correlation location. Then, a weighted least squares fit is performed to find K . Only DD cells that do not correspond to forbidden cells are considered and the weights are chosen as

$$W(\bar{\tau}, \bar{f}_D, t) = \frac{\Gamma(\bar{\tau}, \bar{f}_D, t)}{\max(\Gamma(\bar{\tau}, \bar{f}_D, t))} \quad (8)$$

where Γ is the receiver corrected gain figure accounting for the path losses, receiver antenna gain, and area of the χ^2 footprint. This results in cells with stronger SNR values being weighted more heavily in the fitting. Clutter suppression is only performed for epochs 522 to 538 and 565 to 568 inclusively as the ice-only DDMs have insignificant power away from the specular zone.

To improve the resolution of the spatial image, it is desirable to remove the blurring effect of χ^2 . Due to the irregular mapping of ISO DD lines in the spatial domain, it is simpler to do this in the DD domain to avoid a spatially variant deconvolution problem. We use the Lucy-Richardson method [20], [21] for deconvolution where

$$\hat{Y}_{k+1} = \hat{Y}_k \left(\frac{|Y_{\text{SUP}}(\bar{\tau}, \bar{f}_D, t)|^2}{\hat{Y}_k \otimes \tilde{\chi}^2(\Delta\tau, \Delta f_D)} \otimes \tilde{\chi}^2(-\Delta\tau, -\Delta f_D) \right) \quad (9)$$

is iterated $5 \times$ to estimate the unblurred DDM, \hat{Y}_{DEC} .

For this dataset, only the DDMs (the sDDM [13]) are available, thus, we cannot compensate for this using incoherent range walk compensation [13] so we compensate suboptimally by setting

$$\tilde{\chi}^2(\Delta\tau, \Delta f_D) = \mathcal{F}^{-1} \{ \mathcal{F} \{ \chi^2(\Delta\tau, \Delta f_D) \} H(\omega_\tau, \omega_{f_D}) \} \quad (10)$$

where $\mathcal{F}\{\}$ is the Fourier transform operator, and

$$H(\omega_\tau, \omega_{f_D}) = \int_{-T/2}^{T/2} e^{j2\pi \left(\omega_\tau \frac{d\tau}{dt} + \omega_{f_D} \frac{df_D}{dt} \right)} dt \quad (11)$$

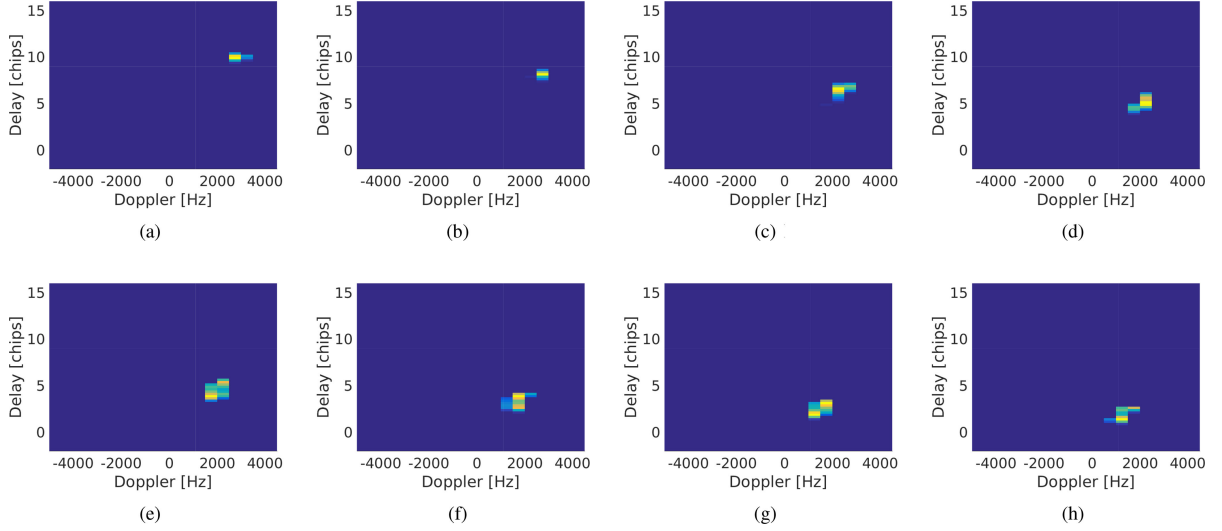


Fig. 8. Mixed DDM sequence after sea clutter suppression, masking, windowing, and deconvolution. These DDMs are depicted in arbitrary units on their own colorscales. (a) Epoch 530. (b) Epoch 531. (c) Epoch 532. (d) Epoch 533. (e) Epoch 534. (f) Epoch 535. (g) Epoch 536. (h) Epoch 537.

is the frequency response of the DD walk blurring kernel and $T = 1$ s is the incoherent integration period. Note that we assume the DCR and DFCR to be constant during the incoherent integration period of the DDM such that the DD walk is approximated with a uniform linear motion of χ^2 . Furthermore, we assume the DFCR to be constant over the entire transition phase, allowing us to use the estimated value shown in Fig. 5(b). Similarly, we also use the estimated DCR in Fig. 5(a) to compute the blurring kernel. However, since the DCR is time variant, we rely not just on the gradient of the fit but also the absolute DD coordinate estimate.

Immediately before deconvolution is performed on the suppressed DDM, the forbidden cells are masked out and a boxcar window is applied. This window is centered at the DD estimate and is ± 1500 Hz by ± 2 chips wide. Fig. 8 shows the processed DDMs from the first transition phase. We can observe that the blurring due to χ^2 and the DD walk has been significantly reduced. Deconvolution is performed on all mixed and ice-only DDMs. However, the ice-only DDMs do not require DD walk compensation as the response originates from the moving specular point that is being tracked by the receiver already.

V. INCOHERENT INTEGRATION

Since the ice response is located on the AFL, we can simply map the power from the DD domain to the spatial domain. This is achieved by a nearest neighbor transformation that is written as

$$\hat{O}(x, y, m) = \hat{Y}_{\text{DEC}}(\tau_{x,y}, f_{D_{x,y}}, m) \quad (12)$$

where

$$\begin{aligned} \tau_{x,y} &= \arg \min_{\bar{\tau}} (\bar{\tau} - \tau(x, y, m)) \\ f_{D_{x,y}} &= \arg \min_{\bar{f}_D} (\bar{f}_D - f_D(x, y, m)) \end{aligned} \quad (13)$$

\hat{O} is an image of the power of the processed DDM projected onto the spatial domain; m is the epoch index in the DDM time series. We then incoherently integrate the \hat{O} image for each DDM in the time series:

$$\bar{O}(x, y) = \sum_{m=1}^M \frac{\hat{O}(x, y, m)}{\max(\hat{O}(x, y, m))} \quad (14)$$

where $M = 47$ is the number of DDMs we are integrating. Furthermore, we normalize each \hat{O} image before integration. This results in the \bar{O} image values being proportional to the dwell time (in the spatial domain) of the response we have tracked throughout the DD domain. Furthermore, the normalization also provides a workaround for the inconsistent magnitude of ice reflections observed by [22]. From this, we expect the value of \bar{O} to be approximately 9 at the edge of the ice sheet given that this is the length of the transition phase shown in Fig. 3. Similarly we expect the value to be 1 along the ice sheet due to the motion of the specular point.

VI. RESULTS

Fig. 9 shows the resultant \bar{O} image after integrating the $M = 47$ \hat{O} images. In this figure, the location of the specular point at each epoch is depicted with a white marker, and, for this dataset, moves from the top left to the bottom right. The shape of the marker indicates the type of DDM corresponding to that epoch: a triangle indicates a clutter-only DDM; a circle indicates a mixed DDM containing clutter and the transitioning ice; and a star indicates a specular ice-only DDM. Fig. 10 shows a slice of the $\bar{O}(x, y)$ image taken along the AFL. In these figures, the \bar{O} image can be considered the step response of the technique proposed in this article to the ice sheet. The first transition phase results in the \bar{O} image having a value of ≈ 11 at the leading edge of the ice sheet that is close to the predicted value of nine corresponding to the length of the first transition phase.

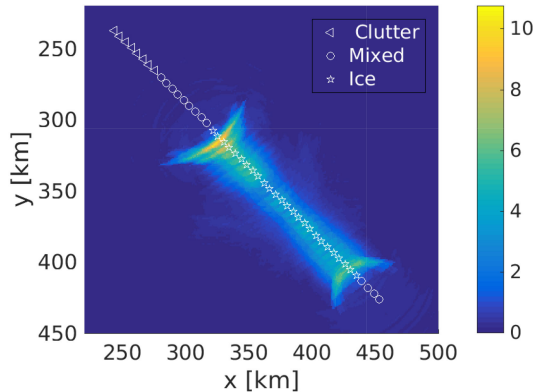


Fig. 9. $\bar{O}(x, y)$ image after integrating all 47 DDMs. The markers indicate the location of the specular point at each epoch that move from the top left to the bottom right chronologically. The edges of the ice sheet along the specular point track are emphasized while the power is spread along the ice sheet.

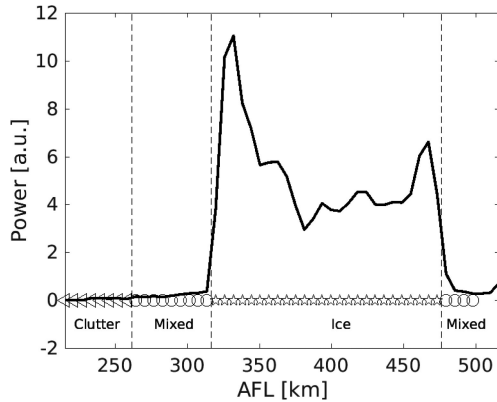


Fig. 10. Slice of the $\bar{O}(x, y)$ image taken along the AFL. This figure clearly shows the emphasis of the ice edge due to the length of the transition phases. The power value is proportional to the dwell time of the ice response.

Imperfect deconvolution and $DD \rightarrow xy$ mapping will cause the \bar{O} values to be higher than those predicted by the dwell time alone. The second transition phase is truncated to just four epochs as the DDMs are extremely noisy after this. Again, the value of \bar{O} at the trailing edge of the ice sheet is commensurate with the dwell time when we consider imperfections in the processing scheme. In these figures, as expected, we can see that during the specular ice-only phase, the power is spread along the AFL due to the motion of the specular point.

VII. DISCUSSION

The cumulative detection of the ice edges due to the integration of the mixed DDMs containing the ice transition phase response improves both the probability of detection and the achievable along-track resolution. Existing methods that classify DDMs as ice do not handle the transition phase and are unable to handle the transition phase. Looking at Fig. 10, we can see that there is potential to detect the location of the edge at a resolution better than the distance between two contiguous specular points, i.e., ≈ 6 km. The accuracy of the estimated location of the edge is affected by, not exhaustively, the transmitter, receiver, and

specular point position errors, improper deconvolution of the DDMs, erroneous mapping back to the spatial domain due to the actual scattering surface not coinciding with the WGS84 ellipsoid and/or errors introduced in the real-time DD tracking scheme. Furthermore, the method presented in this article is a novel processing scheme that exploits the nature of the transition phase in order to obtain a processing gain and an estimator is yet to be derived. As a result, determining the accuracy of the estimated location of the edge of the ice sheet should be carried out in future work wherein an estimator is developed using the spatial domain power maps produced using the method presented in this article.

Since the power is normalized and projected back onto the Earth's surface before integration then it is simple to aggregate multiple observations made by TDS-1 of the same ice sheet but with a diverse range of specular tracks. This would enable the production of maps wherein each track is a different projection (slice) of the ice sheet similar to that shown in Fig. 10. This can easily be extended to integrate DDMs collected by other receivers as the (normalized) power and spatial frame are receiver independent. With sufficient coverage, maps of ice sheets could be produced by aggregating data from a multitude of platforms so long as they are relatively coincident temporally to ensure the ice has not morphed between observations.

The transition phase response of the ice sheet in the mixed DDMs can be attributed to a fixed scattering facet on the surface. We can say this as the DD trajectory matches the dynamics of a point on the AFL. Furthermore, we observe the response suffers from a DD walk that is commensurate with a spatially fixed point-like scatterer. This point-like scattering is characteristic of a coherent reflection. Observation of the DD walk in Fig. 6 experimentally confirms the effect predicted by [13]. Additionally, these observations show that persistent nonspecular forward scattering of GPS signals off ice sheets occurs. Further work is required to investigate these scattering effects and to consolidate them with existing or novel scattering models yet to be developed. This article should investigate the effects of the bistatic geometry with respect to the orientation of the edge of the ice sheet as it may be possible that the origin of the reflection is not completely stationary but moves slightly along the edge of the ice that may contribute to the error between the observed DD trajectory and that expected of a point on the AFL.

The computational cost of the technique presented in this article is relatively high. This is especially true considering that a DDM must be simulated for all those that have clutter suppression applied. Techniques that blindly suppress the sea clutter, e.g., [23], would drastically reduce the computational cost of this technique. Furthermore, the deconvolution operation in the preprocessing stage is implemented with convolution. Since $\tilde{\chi}^2$ is a separable kernel, the 2-D convolution in (9) can be implemented as a series of 1-D convolutions, significantly reducing the computational cost. Additionally, (11) and (10) can be computed *a priori* using the bistatic dynamics extracted from the metadata. These augmentations would reduce the computational cost to a degree where it would be feasible to implement the technique presented in this article in real-time receivers.

VIII. CONCLUSION

In a sequence of DDMs, the transition from open seas to an ice sheet has been shown to have a response that is moving in the DD domain but fixed in the spatial domain. This is the ice edge. A specular ice-only DDM is then observed as the response then comes from the moving specular point. Finally, as the ice sheet leaves the DDM, the response again moves in the DD domain and is fixed in the spatial domain corresponding to the trailing ice edge. In addition to this, the response is bound to the AFL. This allows us to transform the response in all DDMs back to the spatial domain without encountering any ambiguity problems. By incoherently integrating the power after normalization in the spatial domain the resultant image is then proportional to the dwell time (length of transition phase). This results in the edges of the ice sheet being emphasized enabling higher probability of detection and accurate localization estimates.

ACKNOWLEDGMENT

The authors would like to thank the anonymous reviewers for their comments and suggestions which improved the quality of this article. The authors would also like to thank Measurement of Earth Reflected Radio By Satellite (MERRByS) project and Surrey Satellite Technology Limited (SSTL) for making the data collected by TDS-1 available.

REFERENCES

- [1] A. Komjathy, J. Maslanik, V. Zavorotny, P. Axelrad, and S. Katzberg, "Sea ice remote sensing using surface reflected GPS signals," in *Proc. Int. Geosci. Remote Sens. Symp.*, 2000, pp. 2855–2857.
- [2] M. B. Rivas, J. A. Maslanik, and P. Axelrad, "Bistatic scattering of GPS signals off Arctic sea ice," *IEEE Trans. Geosci. Remote Sens.*, vol. 48, no. 3, pp. 1548–1553, Mar. 2010.
- [3] S. Gleason, "Remote sensing of ocean, ice and land surfaces using bistatically reflected GNSS signals from low Earth orbit," Ph.D. dissertation, Univ. Surrey, Guildford, U.K., Dec. 2006.
- [4] D. Masters, P. Axelrad, and S. Katzberg, "Initial results of land-reflected GPS bistatic radar measurements in SMEX02," *Remote Sens. Environ.*, vol. 92, no. 4, pp. 507–520, 2004.
- [5] E. Loria, A. O. Brien, and I. J. Gupta, "Detection & separation of coherent reflections in GNSS-R measurements using CYGNSS data," in *Proc. Int. Geosci. Remote Sens. Symp.*, 2018, pp. 4003–4006.
- [6] Q. Yan and W. Huang, "Spaceborne GNSS-R sea ice detection using delay-Doppler maps: First results from the U.K. TechDemoSat-1 mission," *IEEE J. Sel. Topics Appl. Earth Observ. Remote Sens.*, vol. 9, no. 10, pp. 4795–4801, Oct. 2016.
- [7] A. Alonso-Arroyo, V. U. Zavorotny, and A. Camps, "Sea ice detection using U.K. TDS-1 GNSS-R data," *IEEE Trans. Geosci. Remote Sens.*, vol. 55, no. 9, pp. 4989–5001, Sep. 2017.
- [8] P. M. Woodward, *Probability and Information Theory, With Applications to Radar*. Amsterdam, The Netherlands: Elsevier, 1980.
- [9] A. G. Voronovich and V. U. Zavorotny, "Bistatic radar equation for signals of opportunity revisited," *IEEE Trans. Geosci. Remote Sens.*, vol. 56, no. 4, pp. 1959–1968, Apr. 2018.
- [10] B. J. Southwell, "Investigating the sensitivity of delay Doppler maps to wind direction using ambiguous stare processing," in *Proc. 31st Int. Tech. Meet. Satell. Divis. Inst. Navigat.*, 2018, pp. 2819–2833.
- [11] Y. Zhu, K. Yu, J. Zou, and J. Wickert, "Sea ice detection based on differential delay-Doppler maps from UK TechDemoSat-1," *Sensors (Switzerland)*, vol. 17, no. 7, pp. 1614–1631, 2017.
- [12] D. Schiavulli, F. Frappart, G. Ramillien, J. Darrozes, F. Nunziata, and M. Migliaccio, "Observing sea/ice transition using radar images generated from TechDemoSat-1 delay Doppler maps," *IEEE Geosci. Remote Sens. Lett.*, vol. 14, no. 5, pp. 734–738, May 2017.
- [13] B. J. Southwell and A. G. Dempster, "Incoherent range walk compensation for spaceborne GNSS-R imaging," *IEEE Trans. Geosci. Remote Sens.*, vol. 57, no. 5, pp. 2535–2542, May 2019.
- [14] B. J. Southwell and A. G. Dempster, "An adaptive window for GNSS-R stare processing," in *Proc. IEEE Int. Geosci. Remote Sens. Symp.*, 2019, pp. 8733–8736.
- [15] B. J. Southwell and A. G. Dempster, "A new approach to determine the specular point of forward reflected GNSS signals," *IEEE J. Sel. Topics Appl. Earth Observ. Remote Sens.*, vol. 11, no. 2, pp. 639–646, Feb. 2018.
- [16] J. W. Cheong, "Towards multi-constellation collective detection for weak signals: A comparative experimental analysis," in *Proc. Int. Tech. Meet. Satell. Divis. Inst. Navigat.*, 2011, pp. 3709–3719.
- [17] A. Di Simone, H. Park, D. Riccio, and A. Camps, "Sea target detection using spaceborne GNSS-R delay-Doppler maps: Theory and experimental proof of concept using TDS-1 data," *IEEE J. Sel. Topics Appl. Earth Observ. Remote Sens.*, vol. 10, no. 9, pp. 4237–4255, Sep. 2017.
- [18] B. J. Southwell and A. G. Dempster, "Simulating delay doppler maps of GNSS signals reflected off the ocean surface," in *Proc. Australian Space Res. Conf.*, 2017.
- [19] B. J. Southwell, "Techniques for spaceborne remote sensing of Earth's oceans using reflected GNSS signals," Ph.D. dissertation, School of Electrical Engineering and Telecommunications, Univ. New South Wales, Sydney, Aug. 2019.
- [20] L. B. Lucy, "An iterative technique for the rectification of observed distributions," *Astronomical J.*, vol. 79, pp. 745–754, 1974.
- [21] W. H. Richardson, "Bayesian-based iterative method of image restoration," *J. Opt. Soc. Amer.*, vol. 62, no. 1, pp. 55–59, 1972.
- [22] S. Gleason, "Towards sea ice remote sensing with space detected GPS signals: Demonstration of technical feasibility and initial consistency check using low resolution sea ice information," *Remote Sens.*, vol. 2, no. 8, pp. 2017–2039, 2010.
- [23] J. W. Cheong, B. J. Southwell, and A. G. Dempster, "Blind sea clutter suppression for spaceborne GNSS-R target detection," *IEEE J. Sel. Topics Appl. Earth Observ. Remote Sens.*, to be published.



Benjamin J. Southwell (Student Member, IEEE) received the B.Eng. (Medal) from the University of Western Sydney, Sydney, NSW, Australia, in 2012. He is currently working toward the Ph.D. degree in electrical engineering with the Australian Centre for Space Engineering Research, University of New South Wales, Sydney, NSW, Australia.

His current research interests include remote sensing with reflected Global Navigation Satellite System (GNSS) signals and other signals of opportunity with airborne and spaceborne receivers.



Andrew G. Dempster (Senior Member, IEEE) received the B.E. and M.Eng.Sc. degrees from the University of New South Wales (UNSW), Sydney, NSW, Australia, in 1984 and 1992, respectively, and the Ph.D. degree in efficient circuits for signal processing arithmetic from the University of Cambridge, Cambridge, MA, USA, in 1995.

He is the Director of the Australian Centre for Space Engineering Research (ACSER), UNSW. He was a System Engineer and a Project Manager for the first GPS receiver developed in Australia in the late 80s and has been involved in satellite navigation ever since. He has authored or coauthored in the areas of arithmetic circuits, signal processing, biomedical image processing, satellite navigation, and space systems. His current research interests include satellite navigation receiver design and signal processing, areas where he has six patents, new location technologies, and space systems.